Bioactive Materials 5 (2020) 569–576

Contents lists available at ScienceDirect

Bioactive Materials

journal homepage: http://www.keaipublishing.com/biomat

Bioprinting of radiopaque constructs for tissue engineering and understanding degradation behavior by use of Micro-CT

Sudipto Datta[a], Shuvodeep Jana[c], Ankita Das[a], Arindam Chakraborty[b], Amit Roy Chowdhury[a,b], Pallab Datta[a,*]

[a] Centre for Healthcare Science and Technology, Indian Institute of Engineering Science and Technology, Shibpur, Howrah, 711103, WB, India
[b] Department of Aerospace Engineering and Applied Mechanics, Indian Institute of Engineering Science and Technology, Shibpur, Howrah, 711103, WB, India
[c] Indian Institute of Technology, Kharagpur, West Bengal, India

ARTICLE INFO

Keywords:
Bioprinting
Radiopaque
Barium
Degradation
Cell viability

ABSTRACT

Bioprinting has emerged as a potential technique to fabricate tissue engineering constructs and in vitro models directly using living cells as a raw material for fabrication, conforming to the heterogeneity and architectural complexity of the tissues. In several of tissue engineering and in vitro disease modelling or surgical planning applications, it is desirable to have radiopaque constructs for monitoring and evaluation. In the present work, enhanced radiopaque constructs are generated by substituting Calcium ions with Barium ions for crosslinking of alginate hydrogels. The constructs are characterized for their structural integrity and followed by cell culture studies to evaluate their biocompatibility. This was followed by the radiopacity evaluation. The radiological images obtained by micro-CT technique was further applied to investigate the degradation behavior of the scaffolds. In conclusion, it is observed that barium crosslinking can provide a convenient means to obtain radiopaque constructs with potential for multi-faceted applications.

1. Introduction

Presently, several tissue engineered constructs are under clinical consideration, built upon accumulated in vitro and in vivo evidences over the last three decades [1–3]. Polymeric biomaterials are often the most suitable choice of biomaterials for tissue engineering, especially for soft tissue because of their biodegradability, tailorability of properties, and flexibility of fabrication [4,5]. Elsewhere, radiographic and fluoroscopic visualization is an essential exercise not only for diagnosis but also for the pre-operative planning, image-guided surgeries and assessment of post-surgical outcomes [6–10]. For example, spinal fusion devices are made radiopaque for intra-operative positioning whereas radiopacifiers are routinely added to the methacrylate cements for implant fixation in treatment of compression fractures [11–13]. The need for radiopacity in soft tissue repair is thus increasing [14]. Radiopacity is also emerging as a desired feature for design of polymeric transcatherter heart valves [15–17]. In addition, polymeric phantoms are emergently being employed for patient-specific treatment planning while polymeric embolization coils are also pursued to replace metallic materials [18–21]. However, present major concerns with polymeric tissue engineering are the inability to monitor after implantation, an incomplete comprehension of the rate of degradation behavior of the constructs at implantation site and associated inability to control the degradation at a rate that will match the dynamics of tissue growth. This is attributed to the organic composition resulting in poor radiographic contrast of these materials. This constrains have driven interest for synthesis and modifications to introduce radiopacity in the polymeric materials [14].

Several strategies have been reported in the literature for endowing polymers with radiopaque characteristics. $BaSO_4$, Ta/Bi particles are often embedded in the polymers to impart radiopacity [17,22,23]. Methyl methacrylate monomers when polymerized with zinc or zirconia based acrylates also confers radio-opacity [23–27]. Another common approach has been the grafting of iodine and addition of iodine salts to the polymers. Previously, Ghosh et al. have proposed in situ iodination crosslinking reactions as a promising approach to obtain radiopacity in polysaccharide polymers [28] while Francis et al. extended such an approach for silk visualization [29]. However, nature of mixing of particulate agents results in leakage, sedimentation, andnon-uniform distribution while toxicity concerns of some agents like the aromatic iodinated crosslinking agents have also been raised. Moreover, using the crosslinking reactions for conferring radiopacity alters

Peer review under responsibility of KeAi Communications Co., Ltd.
* Corresponding author.
E-mail addresses: pd@chest.iiests.ac.in, pd@chest.iiests.ac.in (P. Datta).

https://doi.org/10.1016/j.bioactmat.2020.04.015
Received 4 November 2019; Received in revised form 5 April 2020; Accepted 22 April 2020
Available online 27 April 2020

the gelation kinetics and thus may not be suitable for fabrication of all types of polymers.

Recently, bioprinting have emerged as a promising method for fabrication of polymeric implants and surgical models [30–32]. The fabrication modality offers unparalleled opportunity for generating constructs customized for patient specific implantation as well as fabricating cells in living conditions. However, bioprinting is essentially achieved by a sol-gel type of transition of hydrogel polymers within a limited time span. Since the fabrication is performed with living cells, the polymer hydrogel is thus always desired to exhibit a gelation under physiological conditions to avoid damage to cellular components [33]. Such cell-laden hydrogels are often referred to as bioinks and presently there exists a limited repertoire of such cell-friendly bioinks. In the attempt to obtain radiopaque constructs by bioprinting, both particle addition and in situ crosslinking reactions have limited applications since the addition of salt particles modify the flow of complex fluids while crosslinking schemes can deviate the gelation conditions. The polysaccharide polymer, alginate undergoes gelation under physiological conditions and hence, is one of the most commonly explored bioinks [34]. Interestingly, alginate crosslinking is most conveniently performed by the divalent cation Ca^{2+}, though other such cations like Ba^{2+} can also be used as a crosslinker. Ba^{2+} being a heavy atom with radiopacity, in this paper we hypothesized that Ba^{2+} crosslinking can be used to generate radiopaque constructs by bioprinting without disturbing the physiological gelation conditions and maintain cellular vitality during the process [35]. Indeed, Ba^{2+} has been compared to Ca^{2+} with respect to properties of bioplotted constructs but the same has not been investigated for their radiopacity properties. We further evaluate if the same can be applied to study the degradation of the constructs ex vivo or with minimal invasiveness.

Therefore, the Ba^{2+}crosslinked constructs were compared with Ca^{2+} constructs by using micro-CT to study their degradation behavior. Useful insights on the degradation behavior of bioprinted constructs were obtained.

2. Materials and method

2.1. Alginate solution preparation

Sodium alginate salt (2000 cP viscosity, was bought from the (Sigma-Aldrich, USA). The BioInk solution was produced from grade type III ASTM water i.e. (Wasserlab, Spain) . The alginate solution was mixed by mechanical stirring overnight under (Scilogex, USA, 200 rpm) at temperature of (25 °C).

2.2. Extrusion based 3D printer

An extrusion based 3D printer manufactured by M/s Alfatek Systems, India also previously mentioned was used for the printing scaffolds. For slicing the 3D printed solid designed structure by Sketchup 2017, Cura (version 15.04.5, Ultimaker, Netherlands) a software open source was used. Pronterface (version 2014.03.10, Printrun) was used for conversion of the file format from.stl to.GCODE for uploading to the 3D printer.

2.3. Scaffold designing

Sketchup 2017 software was used for designing a 34 mm × 34 mm square solid structure and saved in the format (.stl). CURA an open source software version 15.04.4 was used for slicing the solid printed square structure into mesh type by reducing the fill density from 100% to 18% with printing parameters were taken as follows: strand thickness 2.0, Z-layer stacking and layer upon layer orientation 3.961 mm, strand-to-strand distance 4.4 mm, layer height 0.1 mm, bottom/top thickness 0.6 mm, shell thickness 0.8 mm, filament diameter 1.75 mm, nozzle size 0.41 mm and flow (%) 300. The file is then saved in.GCODE format and loaded in the 3D printer software for printing.

2.4. Printing of alginate ink

The bioink was then filled in a syringe (5 ml) with a nozzle of diameter 0.4 mm attached to it. At a constant printing speed of 50 mm/s the bioink was extruded on the glass petridish (BOROSIL) with a final mesh like construct printed on it at a room temperature 30 °C. Alginate at a concentration of 2.5% w/v was used and in cell-laden bioinks, cells (MG-63) at a concentration of 1 x 10^6 cells/ml was used. As per the required scaffold dimension the printer painted the construct dot by dot. $CaCl_2$ and $BaCl_2$ solutions of 0.5 M each was used to crosslink the respective scaffolds for 2 min, optimized to match the highest viability and structural integrity. For EDX characterization, the final printed scaffolds were washed by ethanol 95% for 3 times including vacuum-dried at a temperature of 40 °C and the amount of Ca/Ba incorporated was quantified by energy dispersive spectroscopy (Zeiss Merlin SEM with an Oxford Instruments EDS detector). The release behaviour of Ca^{2+} and Ba^{2+} was characterized by incubating the samples in distilled water and performing the atomic absorption spectroscopy of the samples obtained by incubating each sample for 3 days.

2.5. Scaffold characterization

The scaffolds images was captured by a digital camera Sony Cybershot (DSC-WX220/B). Axiovision software SE64 Rel 4.9.1 was used for measuring the pore area (PA), strut length (SL) and perimeter of the pore (P). MicroCT GEPhoenix vtomexs voltage 100 KV and current 90 μA was used to CT scan the scaffolds into 1000 slices. Mimics Research 19.0 software was used to measure the Hounsfield unit/Radio opaque, pixel density, porosity and dimension of the struts of the samples. X-Ray (ME X-RAY INDIA PVT LTD ME-5025) voltage 40 kV, current 3 mA and time 2 s was used to take the x-ray images of the scaffolds. Image J open access software was used to determine the intensity of the x-ray images. Tensile testing under uniaxial load was carried out in a Tinius Olsen 5 KT (Tinius Olsen, UK) universal testing machine with 125 N load cell at 0.1 mm/min crosshead speed.. Sample were held using a clip-holder. Samples were loaded at a crosshead speed of 0.1 mm/min. Samples were prestrained for ten cycles with 10% strain before testing.

2.6. Structural accuracy

The structural percentage printing accuracy calculation was done to measure the accuracy of the printed scaffolds with the input design area by using the accuracy matrix mentioned the literature. The two constructs were printed and the printed total area was compared with the total input structure area. The printing accuracy was calculated by using equation (1).

$$\%\ Printing\ accuracy = \left[1 - \frac{Af - Ai}{Ai}\right] \times 100 \quad (1)$$

A_f = Output area (x mm^2)
A_i = input area (756 mm^2)

Structural accuracy of $Ca2^+$ and $Ba2^+$ are 83 ± 0.2 and 79 ± 0.65 respectively.

The bioprinted constructs were also evaluated for the integrity, pore and uniformity factors as proposed by Soltan et al. [36] as follows:

Uniformity Factor (U): This parameter determines the uniformity of the printed strand with the theoretical strand i.e. how uniform the output printed strand is. Printing was done at 50 mm/s. The printed strand is imaged by using optical microscope Nikon Digital camera (NIKON DS-Fi1c, Nikon, Tokyo, Japan). Microscopic image of the strands at various regions were captured and AxioVision SE64 Rel. 4.9.1

software was used to measure the outer edge length of the strand both sides. Uniformity factor was calculated by equation (2) i.e. dividing the printed length with the uniform theoretical length. When the value of U is smaller than 1 then the strand is non-uniform and when it is equal to 1 it is uniform.

$$U = \frac{Printed\ strand\ length}{Theoretical\ strand\ length} \quad (2)$$

Pore Factor (Pr): This parameter determines how close the printed strand pore resembles the structure of the theoretical construct pore i.e. square type. The printing was done at 50 mm/s and the printed pores were imaged by using optical microscope Nikon Digital camera (NIKON DS-Fi1c, Nikon, Tokyo, Japan) at various points and the area as well as the pore perimeter were measured by AxioVision SE64 Rel. 4.9.1 software. The pore parameter was measured by using equation (3). When Pr is less than 1 for under-gelled, Pr value is equal to 1 for properly-gelled and Pr value is greater than 1 for over-gelled of the printed constructs.

$$\mathrm{Pr} = \frac{(Perimeter\ of\ the\ pore)\hat{}2}{16\ \times Area\ of\ pore} \quad (3)$$

Integrity Factor (I): This parameter determines the difference between the printed construct with respect to the desired construct. The 3 layer printed constructed was printed at a printing speed of 50 mm/s and the construct height was imaged by digital camera Sony Cybershot (DSC-WX220/B). By AxioVision SE64 Rel. 4.9.1 software the scaffold height at various points were measured and the compared with a control construct i.e. 5% w/v Alginate which is also printed in the same physical parameters as the other printed construct. The integrity factor is determined by equation (4).

$$I = \frac{Thickness\ of\ the\ construct}{Thickness\ of\ the\ control\ construct} \quad (4)$$

2.7. Cell culture study

Bioprinted scaffolds of dimensions 10 mm × 10 mm, and 100 mm in thickness were produced and kept at 37 °C and 5% CO_2. The cells (MG-63) were maintained in high glucose Dulbecco's modified Eagle's medium (DMEM) supplemented with 10% heat-inactivated fetal bovine serum and 1% penicillin-streptomycin-amphotericin-B antibiotic solution. Cell viability was measured on day 1 and day 3 by 3- [4,5-Dimethylthiazol-2-yl]-2,5-diphenyltetrazolium bromide (MTT) assay (EZcountTM MTT Assay Kit) in a 96 well plate. 10 µl MTT dye was added in 100 µl serum free high glucose DMEM after 24 h and 72 h of cell cultured upon the scaffolds and were incubated for 3 h. 100 µl of solubilization buffer was used to dissolve the formazan crystals that was formed and absorbance was recorded at 570 nm and 670 nm using Multi-Scan Go (Thermo Fisher, Finland) and the percentage of cell viability was calculated according to the manufacturer's protocol. Cell viability was also measured for constructs fabricated with three different concentrations of Ba^{2+}. The cell viability is reported normalized to initial solid surface area of each sample, so that the toxicity of the samples due to the ink components can be compared without scaffold geometries influencing the interpretation. After day 5 of culture, the cells within the constructs were stained with Rhodamine-Phalloidin (Invitrogen, USA) stain for visualizing the cell morphology and incubated for 90 min and washed with 1X PBS thrice. The scaffolds were counterstained with DAPI (λ_{ex} 340–380 nm and λ_{em} 435–485 nm) (Sigma) and observed under inverted fluorescence microscope (Nikon Eclipse TiU, Japan). Live/dead double staining was performed to estimate the number of live and dead cells represented as mean green intensity for quantifying live cells as per the manufacturer's protocol (QIA76 Live/Dead staining kit, Merck Millipore). The green fluorescence (λ_{ex} 465–495 nm and λ_{em} 515–555 nm) was obtained due to the permeability of the dye in case of live cells whereas dead cells were visualized by red fluorescence. The cell images were captured under inverted fluorescence microscope at 20x magnification.

2.8. Alizarin red assay

MG-63 cells in the concentration of $1x10^4$ were seeded upon the scaffolds and cultured for 7 days in high glucose DMEM. 40 mM Alizarin Red S solution was prepared using ASTM Type III water and the scaffolds were stained for 15 min at room temperature. The stained scaffolds were dissolved in 10% acetic acid for 1 h kept on a shaker and the absorbance of the solution was taken at 405 nm in triplicate.

2.9. Statistical analysis

All experiments were performed in triplicate, except Alizarin red assay (n = 5), and mean ± SD values are reported. One-way analysis of the variance along with Bonferroni post hoc test was used to determine the significant differences between the samples and a p value of less than 0.01 was deemed to be significantly different between samples.

3. Results and discussion

3.1. Characterization of bioprinted constructs

Preliminary characterization of the bioprinted constructs obtained by different crosslinkers and depicted in Fig. 1a1-3, was performed using the metrics of Uniformity factor, Integrity factor and Pore factors as described by Soltan et al. [36]. From Fig. 1b, it can be observed that Ca^{2+} crosslinked constructs exhibited better strand width accuracy compared to Ba^{2+} crosslinked constructs. The Ba^{2+} crosslinked constructs tended to flow to higher extent and had higher strand widths compared to Ca^{2+} constructs. On the other hand, the analysis of pore geometry revealed the opposite trend in which pore area of Ca^{2+} constructs was higher compared to Ba^{2+} constructs. Fig. 4 This suggests that crosslinking with Ba^{2+} advanced at a slower pace compared to Ca^{2+}. However, the differences were not very high and in terms of the uniformity and integrity factors, there was no significant differences between the two groups. Similarly, structural accuracy of Ca^{2+} and Ba^{2+} were 83 ± 0.2 and 79 ± 0.65 respectively, which were very close to each other. The differences in the strand width may be due to the differences in the size and diffusion of the ions and slow kinetics of Ba^{2+}. Moreover, different divalent ions are known to possess different affinity for the G and M blocks of the alginate structure [37]. Ideally, if the bioprinted pattern exactly resembles the design, the pores would have been expected to be perfect squares. The pores formed by Ca^{2+} ion showed better square-shaped structures compared to Ba^{2+}. The changes in geometry between the design and bioprinted structures can be attributed tounder- or over-gelation, and can be improved by process parameters as well as modulating the viscosity of the bioink.

3.2. Radiopacity

The aim of the present investigation was to enhance the radiopacity of 3D bioplotted and bioprinted hydrogels. Radiopaque bioprinting will allow fabrication of radiopaque phantoms for surgical planning, as well as allow monitoring of surgical treatment and prognosis through fluoroscopy. Therefore, the visibility of the bioprinted constructs fabricated by Ca and Ba ions were compared. The radiopacity was compared by imaging with a X-ray machine and the Hounsfield unit was calculated. Fig. 2 shows the X-ray films of the Ca^{2+}- (Fig. 2a) and Ba^{2+}-crosslinked (Fig. 2b) scaffolds. The Ba–alginate crosslinked constructs appear brighter than the Ca-crosslinked gel. Further, EDX analysis showed that Ca^{2+} and Ba^{2+} ions were duly incorporated in the scaffolds (Fig. 2c and d). The relative standard deviation of the intensities was further determined at 3 random places in a scaffold and found to be

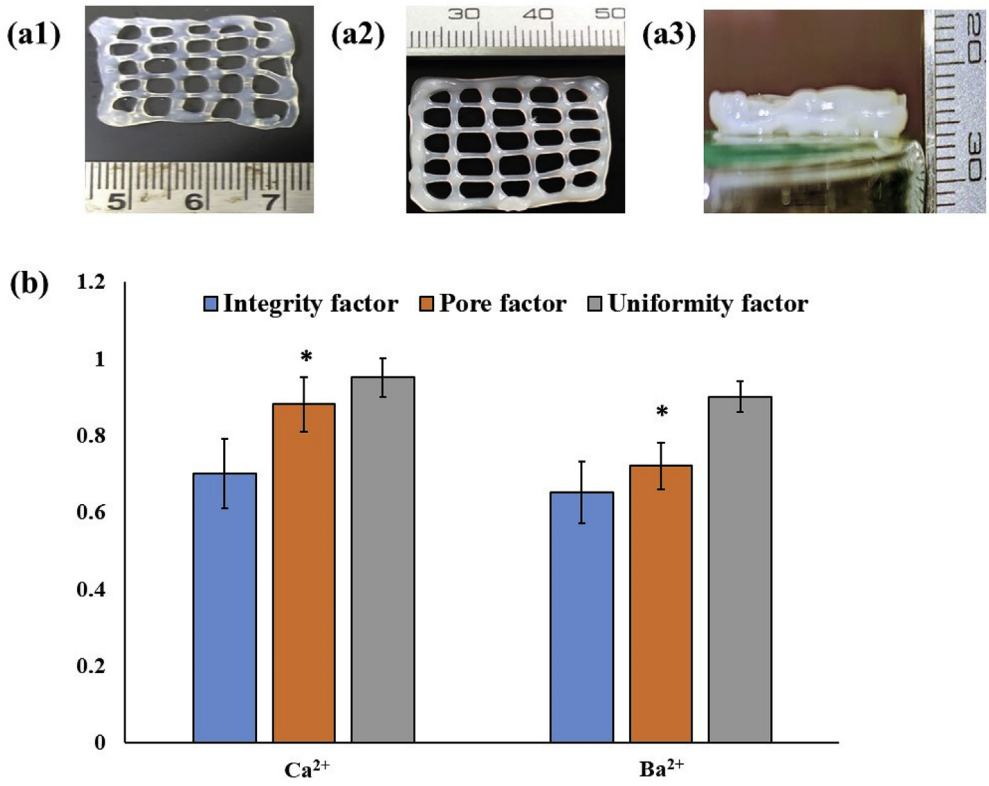

Fig. 1. The photographic images of calcium (a1) and barium (a2) cross-linked scaffolds and (b) comparison of their geometric attributes. * indicates significant difference at $p < 0.01$.

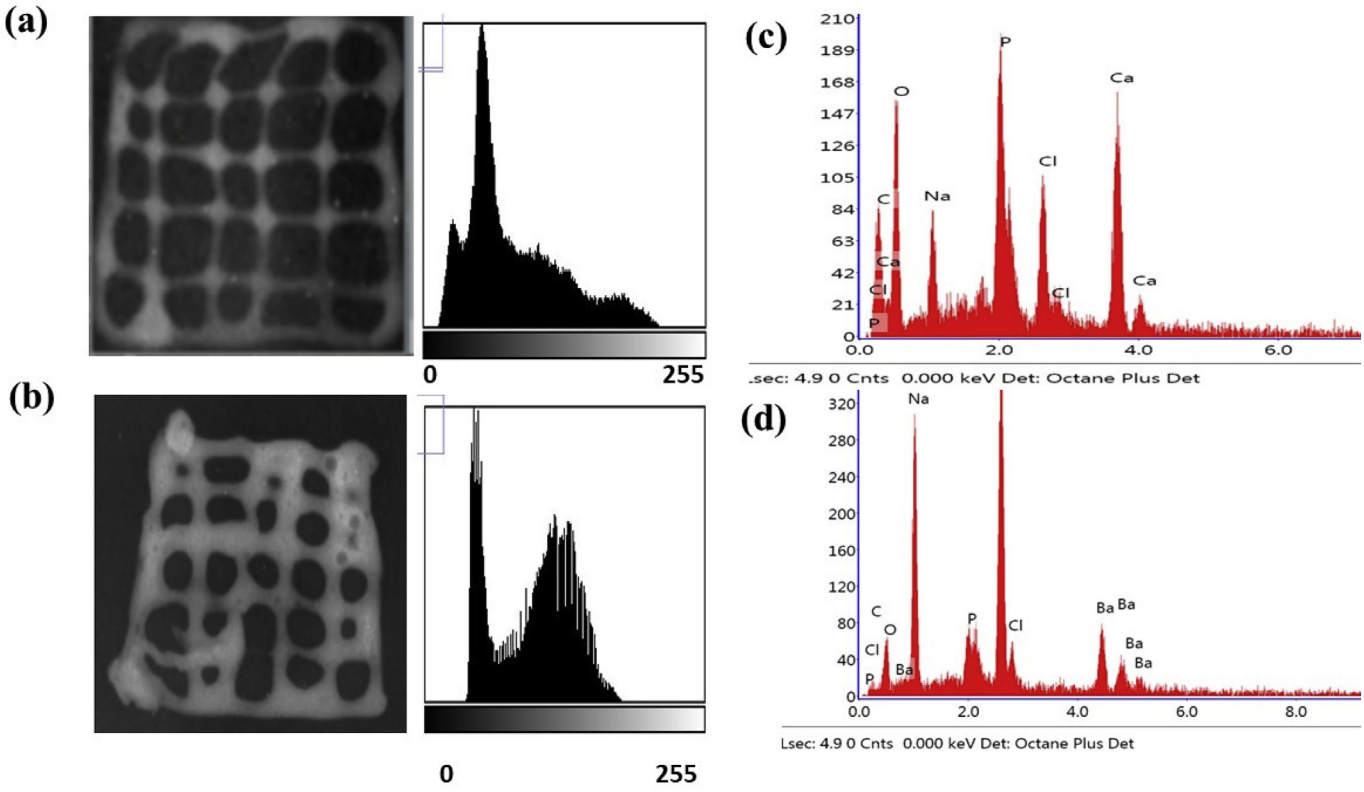

Fig. 2. Radiographic image and corresponding histograph of (a) calcium cross-linked and (b) barium cross-linked scaffolds, (c) EDX spectrum of Ca^{2+} and Ba^{2+} crosslinked scaffolds.

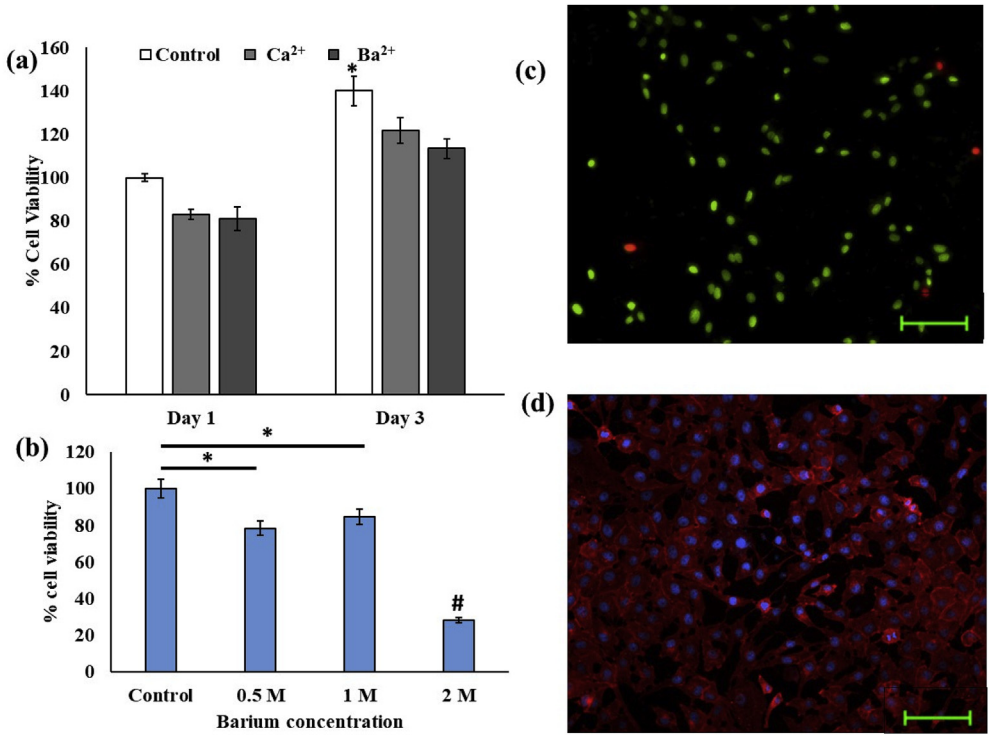

Fig. 3. Cytocompatibility of bioprinted scaffolds evaluated by (a) Cell viability of bioprinted alginate scaffolds cross-linked with calcium and barium cross linkers estimated by MTT assay, and (b) Effect of Barium ions on cell viability in constructs, (c) Live/Dead staining and (d) Rhodamine-phalloidin staining of barium crosslinked constructs. * indicates significant difference at $p < 0.01$. # indicates significant difference at $p < 0.01$ with all other groups.

6.86 ± 1.03% and 6.28 ± 1.17%, depicting sample homogeneity for Ca^{2+} and Ba^{2+} respectively. After three days of incubation, release of the crosslinker ions were monitored and found to be 15.74 ± 0.2 mg/L and 7.44 ± 0.1 mg/L respectively.

To provide a more quantitative analysis, the radio-density of samples was calculated by means of CT value and represented in in Hounsfield scale. The HU of Ca-crosslinked constructs were found to be 88 HU and that of Ba, was 97, indicating a higher radiopacity of the

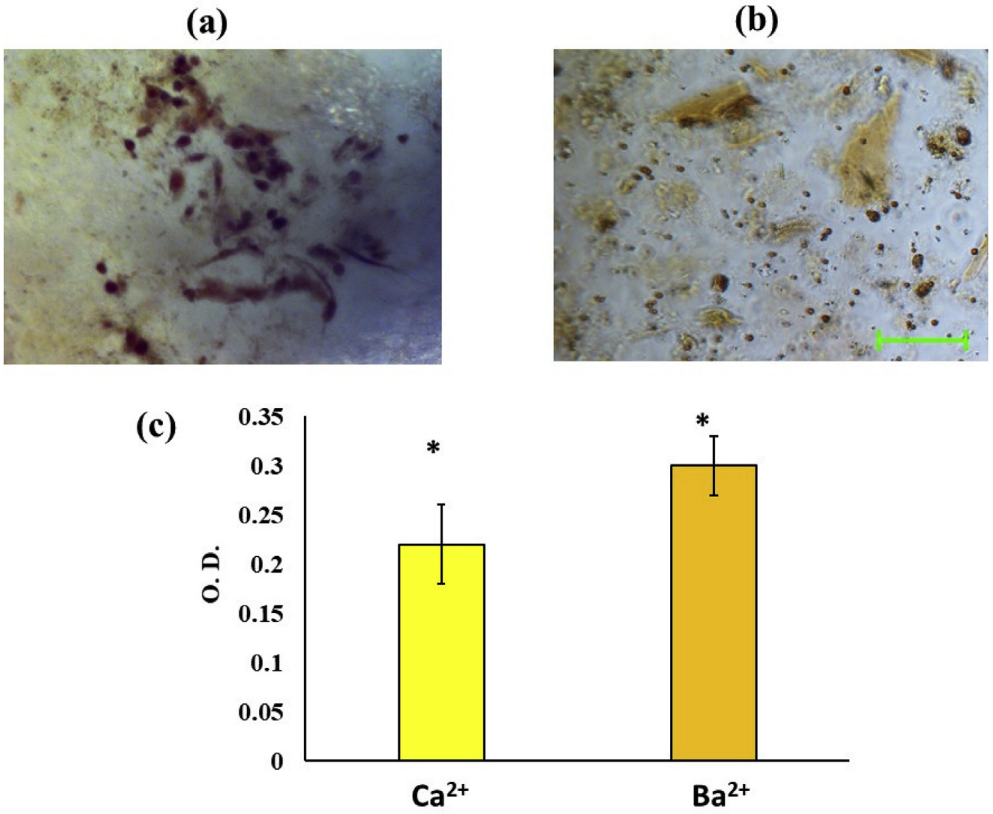

Fig. 4. Bone tissue functionality of bioprinted constructs evaluated by Alizarin red staining showing the stained micrographs of (a1) Calcium and (a2) barium cross-linked scaffolds and (b) their quantitative comparison. Scale bar represents 100 μm and * indicates significant difference at $p < 0.01$.

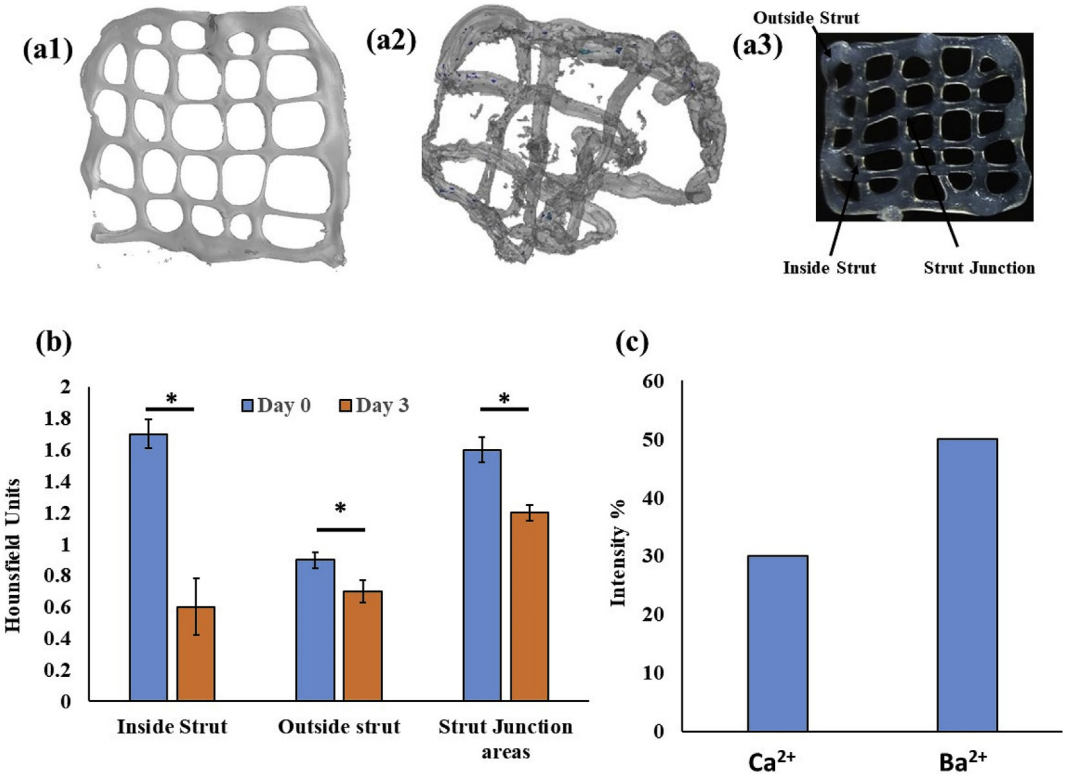

Fig. 5. Degradation of barium crosslinked scaffolds investigated by micro-CT imaging on day 1 (a1), day 3 (a2), designation of the different locations of the scaffolds (a3), (b) the Hounsfiled Unit of the different regions calculated from the micro-CT data and (c) calculated intensity percentages after 28 days of sample degradation. * indicates significant difference at $p < 0.01$.

Barium constructs. From electronic configuration point of view, Ba has higher density than Ca^{2+} and this enables Ba-crosslinked constructs to have a higher radiopacity adequate for thorough visualization of the whole scaffold. In case of Ca^{2+} constructs, not only the average Hu was less, but also the distribution across the whole scaffold geometry was not adequate for visualization. In a previous work, Arifin et al. have shown that Ba^{2+}-crosslinked samples exhibited stable radiopacity for around 15 months in vitro, due to the strong affinity of Ba^{2+} with alginate [26]. However, it should also be noted that differences between Ca^{2+} and Ba^{2+} affinity to alginate is dependent of the relative distribution of G and M block units of alginate. In addition, the mechanical properties of the bioprinted constructs crosslinked with $CaCl_2$ and $BaCl_2$ were evaluated and it was found that the ultimate strength of the constructs was increased in $BaCl_2$ crosslinked constructs (1.6 MPa) compared to the 1.1 MPa obtained for $CaCl_2$ crosslinked scaffolds.

The divalent ions-mediated ionic gelation of alginates has been well studied and attributed to 'egg-box' like structures which are formed where Ca^{2+} ions occupy the cavities and electrostatically bind to poly (guluronate) and poly (mannuronate) moieties of alginate through the negatively charged carboxylate ions. However, poly (mannuronate) blocks have less contribution towards gel formation. Alginate hydrogels coming in contact with PBS, loose the Ca^{2+} ions, present in poly (mannuronate) units, which combine with phosphate ions of PBS to precipitate as salts. Simultaneously, poly (mannuronate) units are dissolved. The Ca^{2+} bound to gluconorate units are extracted in the second phase. However, Ba^{2+} have larger ionic radius and are accommodated more strongly in the poly (guluronate) 'egg-box' cavities, thus undergoing reduced ion-excahnge and maintaining better degradation integrity [38].

3.3. Cell culture

MG 63 cell viability after bioprinting process under the two crosslinkers was evaluated by MTT assay and Live/Dead staining. It was observed that, at the tested concentrations, there was no significant differences between day 1 cell viability in both MTT assay compared to the control group cells cultured on scaffold without bioprinting process, as shown in Fig. 3a. Similarly, on day 3, cell viability was also observed to be equal for both the test groups. This showed that cells can proliferate within the scaffolds in both the tested groups, and maintain viability. Further, it was observed that increasing Ba^{2+} concentration from 0.5 to 1 M did not have a significant effect on cell viability while increasing the concentration to 2 M significantly decreased the cell viability (Fig. 3b). For further experiments, 0.5 M was selected so that constructs can be developed with lowest amount of Ba^{2+} required to provide radiopacity. The cytocompatibility nature of the constructs was further visualized by Live/Dead and rhodamine-phalloidin staining. As depicted in Fig. 3c, Live/Dead staining shows high number of live cells compared to dead cells whereas Fig. 3d depicts the abundant expression of cytoskeleton markers. The results corroborate with the observation of Sarkar et al. who have also found that Ca^{2+} and Ba^{2+} have equal effects during bioprinting with Schwann cells [35]. Similarly, another study reporting bioprinting of U87-MG cells employing a $CaCl_2$– $BaCl_2$ dual crosslinking strategy has also shown that cell viability in 90% range is maintained by this cross-linkers and the developed scaffolds have adequate porosity for cell-cell interactions [39].

After 7 days of culture, the osteogenic marker, Alizarin Red assay was performed for the scaffolds and it was found that the ARS concentration of both the groups expressed ARS higher than the control. As seen from Fig. 4a1-a2 and b, the levels were found to be similar in Ca^{2+}, and Ba^{2+} groups respectively. The results indicate that bioprinted scaffolds can maintain cell functionality. The results of the cell culture study indicate that bioprinted radiopaque scaffolds fabricated by Ba^{2+} crosslinking at the given concentration can maintain viability and functionality of the incorporated cells. Previously, Ba^{2+} ions have shown to be a potential platform for differentiation into bone tissue

[40,41].

3.4. Degradation behaviour

Following the observations that Ba^{2+} crosslinking can provide a biocompatible platform for generating bioprinted radiopaque constructs, the platform was further tested for modeling the degradation behavior of the constructs by micro-CT imaging. The micro-CT images of Ba-crosslinked constructs were sharp and well suited for calculation of Hounsfield units at the various locations of the constructs. It was seen that on day 0, immediately after bioprinting the inside struts, outside struts, and the strut joints had a Hounsfield units of 1.7, 0.9 and 1.6, respectively. On day 3, the same was found to be 0.6, 0.7 and 1.2 units respectively. These results show that bioprinted constructs have highest mass density at the struts joints followed by outside strut regions. Moreover, the degradation rate is also slower in the strut joints compared to both the inside strut regions and the outside strut regions. Moreover, the degradation rate is fastest in the inside strut region, which show a rapid degradation in a 3 day period. After 28 days of incubation, 30 and 50% intensities were measured for calcium and barium crosslinked constructs respectively (Fig. 5c).

These results show that bioprinted constructs are not always uniform and diffusion inside the constructs may be responsible for differential distribution of the polymer-ions at different regions. Moreover, the constructs most likely degrade at different rates at different regions and this may also lead to enhanced diffusion rates inside the constructs over a period of time [42–44].

4. Conclusions and future perspectives

Radiopaque alginate constructs were fabricated by employing a low-cost bioprinting technique. Using Barium ions for crosslinking in comparison to Calcium ions significantly improved the radiopacity without compromising the structural integrity of cell viability to any significant effect. Using a high concentration of calcium ions can cause osmotic effects and result in cell deaths. In addition, the micro-CT images of the scaffolds were found to be useful for understanding the degradation behavior of the scaffolds and indicate inhomogeneous degradation from different parts of the scaffolds may be possible. The work will be extended to develop radiopaque phatoms for surgical planning as well as in vivo monitoring and modelling of scaffold degradation behavior in future.

CRediT authorship contribution statement

Sudipto Datta: Investigation, Methodology. **Shuvodeep Jana:** Investigation, Methodology. **Ankita Das:** Investigation, Methodology. **Arindam Chakraborty:** Investigation, Methodology. **Amit Roy Chowdhury:** Formal analysis, Project administration, Supervision. **Pallab Datta:** Conceptualization, Formal analysis, Funding acquisition, Methodology, Project administration, Resources, Supervision, Writing - original draft, Writing - review & editing.

Declaration of competing interest

Authors declare no conflict of interest.

Acknowledgements

SD thank the Institute Fellowship of IIEST Shibpur. PD thanks the DST for Inspire faculty Award IFA-12-LSBM-48.

References

[1] C.H. Evans, Barriers to the clinical translation of orthopedic tissue engineering, Tissue Eng. B Rev. 17 (2011) 437–441, https://doi.org/10.1089/ten.teb.2011.0228.
[2] S.G. Kwon, Y.W. Kwon, T.W. Lee, G.T. Park, J.H. Kim, Recent advances in stem cell therapeutics and tissue engineering strategies, Biomater. Res. 22 (2018) 36, https://doi.org/10.1186/s40824-018-0148-4.
[3] B.T. O'Donnell, C.J. Ives, O.A. Mohiuddin, B.A. Bunnell, Beyond the present constraints that prevent a wide spread of tissue engineering and regenerative medicine approaches, Front. Bioeng. Biotechnol. 7 (2019) 95, https://doi.org/10.3389/fbioe.2019.00095.
[4] R.L. Heise, B. Adam Blakeney, R.A. Pouliot, F. Puoci (Ed.), Polymers in Tissue Engineering BT - Advanced Polymers in Medicine, Springer International Publishing, Cham, 2015, pp. 177–217, , https://doi.org/10.1007/978-3-319-12478-0_7.
[5] N. Iqbal, A.S. Khan, A. Asif, M. Yar, J.W. Haycock, I.U. Rehman, Recent concepts in biodegradable polymers for tissue engineering paradigms: a critical review, Int. Mater. Rev. 64 (2019) 91–126, https://doi.org/10.1080/09506608.2018.1460943.
[6] J.T. Martin, A.H. Milby, K. Ikuta, S. Poudel, C.G. Pfeifer, D.M. Elliott, H.E. Smith, R.L. Mauck, A radiopaque electrospun scaffold for engineering fibrous musculoskeletal tissues: scaffold characterization and in vivo applications, Acta Biomater. 26 (2015) 97–104, https://doi.org/10.1016/j.actbio.2015.08.001.
[7] B. Chevalier, A. Abizaid, D. Carrié, N. Frey, M. Lutz, J. Weber-Albers, D. Dudek, S.C. Weng, M. Akodad, J. Anderson, G.W. Stone, Null null, clinical and angiographic outcomes with a novel radiopaque sirolimus-eluting bioresorbable vascular scaffold, Circ. Cardiovasc. Interv. 12 (2019) e007283, , https://doi.org/10.1161/CIRCINTERVENTIONS.118.007283.
[8] S. Shen, H. Wang, Y. Xue, L. Yuan, X. Zhou, Z. Zhao, E. Dong, B. Liu, W. Liu, B. Cromeens, B. Adler, G. Besner, R.X. Xu, Freeform fabrication of tissue-simulating phantom for potential use of surgical planning in conjoined twins separation surgery, Sci. Rep. 7 (2017) 11048, https://doi.org/10.1038/s41598-017-08579-6.
[9] E. George, P. Liacouras, T.C. Lee, D. Mitsouras, 3D-Printed patient-specific models for CT- and MRI-guided procedure planning, AJNR. Am. J. Neuroradiol. 38 (2017) E46–E47, https://doi.org/10.3174/ajnr.A5189.
[10] B.A. Hamedani, A. Melvin, K. Vaheesan, S. Gadani, K. Pereira, A.F. Hall, Three-dimensional printing CT-derived objects with controllable radiopacity, J. Appl. Clin. Med. Phys. 19 (2018) 317–328, https://doi.org/10.1002/acm2.12278.
[11] M. Makita, K. Yamakado, A. Nakatsuka, H. Takaki, T. Inaba, F. Oshima, H. Katayama, K. Takeda, Effects of barium concentration on the radiopacity and biomechanics of bone cement: experimental study, Radiat. Med. 26 (2008) 533–538, https://doi.org/10.1007/s11604-008-0269-0.
[12] E.E. Rutherford, L.J. Tarplett, E.M. Davies, J.M. Harley, L.J. King, Lumbar spine fusion and stabilization: hardware, techniques, and imaging appearances, Radiographics 27 (2007) 1737–1749, https://doi.org/10.1148/rg.276065205.
[13] C.S.J. van Hooy-Corstjens, Y.B.J. Aldenhoff, M.L.W. Knetsch, L.E. Govaert, E. Arin, H. Erli, L.H. Koole, Radiopaque polymeric spinal cages: a prototype study, J. Mater. Chem. 14 (2004) 3008–3013, https://doi.org/10.1039/B407228F.
[14] Y. Yang, S.M. Dorsey, M.L. Becker, S. Lin-Gibson, G.E. Schumacher, G.M. Flaim, J. Kohn, C.G. Simon Jr., X-ray imaging optimization of 3D tissue engineering scaffolds via combinatorial fabrication methods, Biomaterials 29 (2008) 1901–1911, https://doi.org/10.1016/j.biomaterials.2007.12.042.
[15] E.M.A. Wiegerinck, F. Van Kesteren, M.S. Van Mourik, M.M. Vis, J. Baan Jr., An up-to-date overview of the most recent transcatheter implantable aortic valve prostheses, Expet Rev. Med. Dev. 13 (2016) 31–45, https://doi.org/10.1586/17434440.2016.1120665.
[16] D. Pavcnik, K.C. Wright, S. Wallace, Development and initial experimental evaluation of a prosthetic aortic valve for transcatheter placement, Work in progress., Radiology. 183 (1992) 151–154, https://doi.org/10.1148/radiology.183.1.1549662.
[17] L. Tian, L. Lu, J. Feng, M.P. Melancon, Radiopaque nano and polymeric materials for atherosclerosis imaging, embolization and other catheterization procedures, Acta Pharm. Sin. B. 8 (2018) 360–370, https://doi.org/10.1016/j.apsb.2018.03.002.
[18] F. Adams, T. Qiu, A. Mark, B. Fritz, L. Kramer, D. Schlager, U. Wetterauer, A. Miernik, P. Fischer, Soft 3D-printed phantom of the human kidney with collecting system, Ann. Biomed. Eng. 45 (2017) 963–972, https://doi.org/10.1007/s10439-016-1757-5.
[19] K.M. Meess, R.L. Izzo, M.L. Dryjski, R.E. Curl, L.M. Harris, M. Springer, A.H. Siddiqui, S. Rudin, C.N. Ionita, 3D printed abdominal aortic aneurysm phantom for image guided surgical planning with a patient specific fenestrated endovascular graft system, Proc. SPIE–the Int. Soc. Opt. Eng. 10138 (2017) 101380P, https://doi.org/10.1117/12.2253902.
[20] J.N. Rodriguez, W. Hwang, J. Horn, T.L. Landsman, A. Boyle, M.A. Wierzbicki, S.M. Hasan, D. Follmer, J. Bryant, W. Small, D.J. Maitland, Design and biocompatibility of endovascular aneurysm filling devices, J. Biomed. Mater. Res. A. 103 (2015) 1577–1594, https://doi.org/10.1002/jbm.a.35271.
[21] P. Jahnke, F.R.P. Limberg, A. Gerbl, G.L. Ardila Pardo, V.P.B. Braun, B. Hamm, M. Scheel, Radiopaque three-dimensional printing: a method to create realistic CT phantoms, Radiology 282 (2016) 569–575, https://doi.org/10.1148/radiol.2016152710.
[22] X. Guo, Radiopaque, barium sulfate-filled biomedical compounds of a poly(ether-block-amide) copolymer, J. Appl. Polym. Sci. 109 (2008) 4015–4024, https://doi.org/10.1002/app.28505.
[23] M.A. Húngaro Duarte, G.D. de Oliveira El Kadre, R.R. Vivan, J.M. Guerreiro Tanomaru, M.T. Filho, I.G. de Moraes, Radiopacity of portland cement associated with different radiopacifying agents, J. Endod. 35 (2009) 737–740, https://doi.org/10.1016/j.joen.2009.02.006.
[24] R. Gillani, B. Ercan, A. Qiao, T.J. Webster, Nanofunctionalized zirconia and barium sulfate particles as bone cement additives, Int. J. Nanomed. 5 (2010) 1–11 https://

www.ncbi.nlm.nih.gov/pubmed/20161983.
[25] N.W. Elshereksi, S.H. Mohamed, A. Arifin, Z.A.M. Ishak, Evaluation of the mechanical and radiopacity properties of poly(methyl methacrylate)/barium titanate-denture base composites, Polym. Polym. Compos. 24 (2016) 365–374, https://doi.org/10.1177/096739111602400507.
[26] D.R. Arifin, S. Manek, E. Call, A. Arepally, J.W.M. Bulte, Microcapsules with intrinsic barium radiopacity for immunoprotection and X-ray/CT imaging of pancreatic islet cells, Biomaterials 33 (2012) 4681–4689, https://doi.org/10.1016/j.biomaterials.2012.03.008.
[27] Q. Wang, K. Qian, S. Liu, Y. Yang, B. Liang, C. Zheng, X. Yang, H. Xu, A.Q. Shen, X-ray visible and uniform alginate microspheres loaded with in situ synthesized BaSO4 nanoparticles for in vivo transcatheter arterial embolization, Biomacromolecules 16 (2015) 1240–1246, https://doi.org/10.1021/acs.biomac.5b00027.
[28] P. Ghosh, M. Das, A.P. Rameshbabu, D. Das, S. Datta, S. Pal, A.B. Panda, S. Dhara, Chitosan derivatives cross-linked with iodinated 2,5-Dimethoxy-2,5-dihydrofuran for non-invasive imaging, ACS Appl. Mater. Interfaces 6 (2014) 17926–17936, https://doi.org/10.1021/am504655v.
[29] N.K. Francis, H.S. Pawar, P. Ghosh, S. Dhara, In situ iodination cross-linking of silk for radio-opaque antimicrobial surgical sutures, ACS Biomater. Sci. Eng. 2 (2016) 188–196, https://doi.org/10.1021/acsbiomaterials.5b00327.
[30] B. Duan, L.A. Hockaday, K.H. Kang, J.T. Butcher, 3D Bioprinting of heterogeneous aortic valve conduits with alginate/gelatin hydrogels, J. Biomed. Mater. Res. 101A (2013) 1255–1264, https://doi.org/10.1002/jbm.a.34420.
[31] A.N. Leberfinger, S. Dinda, Y. Wu, S. V Koduru, V. Ozbolat, D.J. Ravnic, I.T. Ozbolat, Bioprinting functional tissues, Acta Biomater. 95 (2019) 32–49, https://doi.org/10.1016/j.actbio.2019.01.009.
[32] A. Satpathy, P. Datta, Y. Wu, B. Ayan, E. Bayram, I.T. Ozbolat, Developments with 3D bioprinting for novel drug discovery, Expet Opin. Drug Discov. 13 (2018) 1115–1129, https://doi.org/10.1080/17460441.2018.1542427.
[33] P. Datta, A. Barui, Y. Wu, V. Ozbolat, K.K. Moncal, I.T. Ozbolat, Esssential steps in bioprinting: from pre- to post-bioprinting, Biotechnol. Adv. 36 (2018) 1481–1504.
[34] S. Datta, A. Das, P. Sasmal, S. Bhutoria, A. Roy Chowdhury, P. Datta, Alginate- poly (amino acid) extrusion printed scaffolds for tissue engineering applications, Int. J. Polym. Mater. Polym. Biomater. 69 (2020) 65–72.
[35] M. Sarker, M. Izadifar, D. Schreyer, X. Chen, Influence of ionic crosslinkers (Ca2+/Ba2+/Zn2+) on the mechanical and biological properties of 3D Bioplotted Hydrogel Scaffolds, J. Biomater. Sci. Polym. Ed. 29 (2018) 1126–1154, https://doi.org/10.1080/09205063.2018.1433420.
[36] N. Soltan, L. Ning, F. Mohabatpour, P. Papagerakis, X. Chen, Printability and cell viability in bioprinting alginate dialdehyde-gelatin scaffolds, ACS Biomater. Sci. Eng. 5 (2019) 2976–2987, https://doi.org/10.1021/acsbiomaterials.9b00167.
[37] Ý.A. Mørch, I. Donati, B.L. Strand, Effect of Ca2+, Ba2+, and Sr2+ on alginate microbeads, Biomacromolecules 7 (2006) 1471–1480, https://doi.org/10.1021/bm060010d.
[38] M. Bajpai, P. Shukla, S.K. Bajpai, Ca(II)+Ba(II) ions crosslinked alginate gels prepared by a novel diffusion through dialysis tube (DTDT) approach and preliminary BSA release study, Polym. Degrad. Stabil. 134 (2016) 22–29, https://doi.org/10.1016/j.polymdegradstab.2016.09.027.
[39] A.G. Tabriz, M.A. Hermida, N.R. Leslie, W. Shu, Three-dimensional bioprinting of complex cell laden alginate hydrogel structures, Biofabrication 7 (2015) 045012.
[40] G. Wang, W. Su, P. Chen, T. Huang, Divalent metal ions induced osteogenic differentiation of MC3T3E1, IOP Conf. Ser. Mater. Sci. Eng. 275 (2017) 12004, https://doi.org/10.1088/1757-899x/275/1/012004.
[41] H. Alizadeh Sardroud, S. Nemati, A. Baradar Khoshfetrat, M. Nabavinia, Y. Beygi Khosrowshahi, Barium-cross-linked alginate-gelatine microcapsule as a potential platform for stem cell production and modular tissue formation, J. Microencapsul. 34 (2017) 488–497, https://doi.org/10.1080/02652048.2017.1354940.
[42] S. Zheng, Z. Li, Z. Liu, The inhomogeneous diffusion of chemically crosslinked Polyacrylamide hydrogel based on poroviscosity theory, Sci. China Technol. Sci. 62 (2019) 1375–1384, https://doi.org/10.1007/s11431-018-9472-2.
[43] H. Nitzsche, H. Metz, A. Lochmann, A. Bernstein, G. Hause, T. Groth, K. Mäder, Characterization of scaffolds for tissue engineering by benchtop-magnetic resonance imaging, Tissue Eng. C Methods 15 (2009) 513–521, https://doi.org/10.1089/ten.tec.2008.0488.
[44] G. Skjåk-Bræk, H. Grasdalen, O. Smidsrød, Inhomogeneous polysaccharide ionic gels, Carbohydr. Polym. 10 (1989) 31–54, https://doi.org/10.1016/0144-8617(89)90030-1.